Available online at www.sciencedirect.com
SCIENCE DIRECT®
International Journal of Solids and Structures 43 (2006) 2014–2036
INTERNATIONAL JOURNAL OF SOLIDS and STRUCTURES
www.elsevier.com/locate/ijsolstr

Role of plasticity on indentation behavior: Relations between surface and subsurface responses

Ivindra Pane *, Eberhard Blank

Computational Materials Laboratory, Institute of Materials, Swiss Federal Institute of Technology, CH-1015 Lausanne, Switzerland

Received 9 December 2004
Available online 21 October 2005

Abstract

Surface and subsurface responses during frictionless indentation of elasto-plastic solids are investigated. Cases of monotonic and repeated loading are considered. It is shown that the role of plasticity parameters on indentation behavior cannot be well described in terms of surface response alone. It must be tied with subsurface response. In particular, the difference between the materials exhibiting isotropic hardening and that exhibiting kinematic hardening is less apparent when the force-displacement response and the deformed surface from the two are compared. Yet, it is quite apparent when subsurface response such as plastic strain, residual stress and plastic zone dimension are compared. An attempt has been made to characterize such surface and subsurface responses, for different plastic behavior, and to compare them with estimations obtained from analytical solutions.

Keywords: Substrate; Plasticity

1. Introduction

Many situations involving elasto-plastic contact behavior exist in manufacturing, fabrication, and packaging processes, as well as in structural and mechanical systems. Elasto-plastic contact behavior also plays a key role in damage modes involving wear and friction often occurring in the above processes and systems. However, in the examples above the contact loading is seldom described by quantities derived from elasto-plastic contact behavior. Rather, contact loading and the material response at the surface are treated empirically in terms of hardness or indentation strain. The latter may represent the averaged material behavior but may not capture the important mechanisms responsible for material failures.

Although a number of studies have been dedicated to analyzing elasto-plastic indentation, the quantification of some representative surface and subsurface responses is not an easy task. In the early 1950s, based on the work of Meyer (1908) and Tabor (1951) substantiated quantities like hardness and indentation strain. These are surface responses that are believed to represent the material response involving elasto-plastic

* Corresponding author.
E-mail addresses: ivindra.pane@epfl.ch, ivpane@netscape.net (I. Pane).

0020-7683/$ - see front matter © 2005 Elsevier Ltd. All rights reserved.
doi:10.1016/j.ijsolstr.2005.08.010

indentation. Tabor's study and more recent studies (Park and Pharr, 2004; Mesarovic and Fleck, 1999; Yu and Blanchard, 1996) also imply that plastic and hardening behavior may not be well captured simply by surface response like a single-valued hardness, instead by hardness-indentation strain relations. Such relations obtained from spherical indentation have been shown to capture differences caused by different plastic and hardening behavior (Tabor, 1951; Tirupataiah and Sundararajan, 1991). This has been the basis for a method to infer the stress–strain relation of metallic materials (Tabor, 1951; Tirupataiah and Sundararajan, 1991, 1987, 1994). However, such a method is subject to some criticisms mainly due to the inaccuracy of the measured contact radius, and it has not been applied for a wide variety of elasto-plastic materials. Nevertheless, it is important to understand thoroughly the relation between hardness and indentation strain for materials with different hardening and plastic behavior. One way to do this is using the finite element simulation where the contact radius developing during indentation can be monitored accurately.

Since many technologically important materials including steels, cemented carbide, aluminum, copper, nickel, and their alloys exhibit different hardening behavior it appears necessary to study indentation responses as affected by hardening. This means that phenomena exhibited by the kinematic hardening such as Bauschinger effect and ratchetting, in addition to the classical isotropic hardening behavior, need to be investigated. Furthermore, to capture the complex effect of kinematic hardening, the investigation must be extended to the case of cyclic indentation loading. Indentation responses to be analyzed also need to be broadened to include, not only the surface response such as hardness-indentation strain, but also the subsurface response such as distributions and development of plastic strains, stresses, and plastic zone. While many investigations have been done to study the surface response by indentation (Tabor, 1951; Park and Pharr, 2004; Tirupataiah and Sundararajan, 1991, 1987, 1994; Jayaraman et al., 1998; Bhattacharya and Nix, 1988), very little is known about the subsurface response. This is not surprising because the indentation experiment measures only the surface response in terms of the load–displacement curve and the deformed surface profile. Some studies on the subsurface response have shed some light on the stress and strain distributions as well as on the size or shape of plastic zone (Hardy et al., 1971; Kral et al., 1993; Samuels and Mulhearn, 1956; Koeppel and Subhash, 1999). Since correlations between the surface and subsurface responses are still lacking, our intent here is to elaborate on such correlations and to see whether some important links can be made.

Capturing and modeling different hardening behavior at the continuum level remains a non-exhausted subject of research. Models have been developed to incorporate cyclic plasticity behavior which, according to Suresh (1998) should include the Bauschinger effect, elastic shakedown, cyclic hardening or softening, ratchetting, and mean stress relaxation (Armstrong and Frederick, 1966; White et al., 1990; Bower, 1989; Jiang and Sehitoglu, 1996,a,b; Mizuno et al., 2000; Ohno and Abdel-Karim, 2000; Ekh et al., 2000). Some of these models are very versatile and capture the aforementioned behavior. Many have been extended from a known kinematic hardening model by Armstrong and Frederick (1966). Evaluation of different hardening models is beyond the scope of this paper. Here, we limit our effort to elasto-plastic indentation simulations using a J_2-flow plasticity model with combined isotropic–kinematic hardening that enable us to capture Bauschinger effect, ratchetting and shakedown. Such a model has been presented and used by, among others, White et al. (1990), Ekh et al. (2000), and Pedersen (2000) for problems other than indentation. It appears to be satisfactory and capable of capturing the important aspects of cyclic hardening behavior.

It is worth mentioning that while there have been studies using the isotropic hardening plasticity (Bhattacharya and Nix, 1988; Kral et al., 1993), applications of cyclic hardening plasticity, and in particular using the combined isotropic–kinematic hardening to elasto-plastic contact problems are still rare. Investigations on how the isotropic and kinematic hardening models affect the spherical indentation behavior have been done by Huber and Tsakmakis (1998, 1999a,b) who emphasized more on extracting material properties but included some analysis on surface and subsurface responses.

This paper aims at studying the normal frictionless indentation behavior of homogeneous metallic substrates as influenced by their elasto-plastic parameters, and by no means covers all aspects related to constitutive modeling of materials and elasto-plastic indentation behavior. It focuses on studying some characteristic surface response due to spherical indentation, such as the variation of mean pressure (Meyer hardness) with indentation strain, and its relation to the subsurface response including the plastic zone dimension, plastic strain and residual stress. This is done primarily for the case of monotonic loading, where the role of plasticity parameters of different hardening behavior can be generalized and examined. Then, an analysis

is performed for two cases of cyclic loading, where different hardening behavior (and their corresponding plasticity parameters) are examined in terms of load–displacement curve and subsurface stress and strain. Studies of this kind appear to be new since previous work focuses mainly on indentation behavior with isotropic hardening plasticity (Mesarovic and Fleck, 1999; Bhattacharya and Nix, 1988; Hardy et al., 1971; Kral et al., 1993) or on extracting isotropic and kinematic hardening properties using the indentation method (Huber and Tsakmakis, 1999a,b; Bucaille et al., 2003; Dao et al., 2001). Studies by Huber and Tsakmakis (1998, 1999b) are among those that emphasize the importance of the effect of the combined hardening behavior. It is believed that through this paper a novel implementation of the combined isotropic–kinematic hardening plasticity will allow to further study numerically the roles of plastic parameters and hardening on indentation behavior. The model, as has been applied to the experimental data in Appendix A, can deal with different phenomena, such as Bauschinger effect and ratchetting whose influences are obvious in deformation modes other than the indentation test, e.g. tensile or bending test.

2. Constitutive law and model

2.1. Combined isotropic–kinematic hardening plasticity

We consider here a J_2-flow plastic constitutive law described in the rate form as:

$$\boldsymbol{D} = \boldsymbol{D}^e + \boldsymbol{D}^p \tag{1}$$

where $\boldsymbol{D}$ denotes the symmetric part of the of velocity gradient. The relation above was obtained from the multiplicative plasticity theory where the multiplicative decomposition of the deformation gradient into elastic and plastic parts (Belytschko et al., 2001) holds, $\boldsymbol{F} = \boldsymbol{F}^e \cdot \boldsymbol{F}^p$. Accordingly, the spatial velocity gradient is written,

$$\boldsymbol{L} = \dot{\boldsymbol{F}} \cdot \boldsymbol{F}^{-1} = \dot{\boldsymbol{F}}^e \cdot (\boldsymbol{F}^e)^{-1} + \boldsymbol{F}^e \cdot \dot{\boldsymbol{F}}^p \cdot (\boldsymbol{F}^p)^{-1} \cdot (\boldsymbol{F}^e)^{-1} = \boldsymbol{L}^e + \boldsymbol{F}^e \cdot \boldsymbol{L}^p \cdot (\boldsymbol{F}^e)^{-1} \tag{2}$$

Notice that in the case of metallic materials where the elastic deformation is small compared to the plastic deformation, (2) simplifies to

$$\boldsymbol{L} \approx \boldsymbol{L}^e + \boldsymbol{L}^p \tag{3}$$

Furthermore, the velocity gradient tensor can be decomposed into symmetric ($\boldsymbol{D}$) and antisymmetric parts ($\boldsymbol{W}$),

$$\boldsymbol{L} = \left(\frac{\partial v}{\partial \boldsymbol{x}}\right)^{\mathrm{T}} = \boldsymbol{D} + \boldsymbol{W} \tag{4}$$

Considering the symmetric part of this equation one can recover (1).

We follow the approach outlined in Weber (1988) and Weber et al. (1988), which was also described by White (1988) and White et al. (1990), to extend the small deformation version of a constitutive law to its large deformation version. In such an approach, the tangent moduli relates an objective rate called Jaumann rate $\check{()}$ is used, of a stress tensor with the deformation,

$$\check{\boldsymbol{\tau}} = \boldsymbol{C}^e : (\boldsymbol{D} - \boldsymbol{D}^p), \quad \check{\boldsymbol{\tau}} = \dot{\boldsymbol{\tau}} - \boldsymbol{W}.\boldsymbol{\tau} - \boldsymbol{\tau}.\boldsymbol{W}^{\mathrm{T}} \tag{5}$$

The stress tensor is chosen to be Kirchoff stress because it leads to symmetric tangent moduli (Belytschko et al., 2001),

$$\boldsymbol{\tau} = J\sigma, \quad J = \det \boldsymbol{F} \tag{6}$$

The elastic behavior is isotropic with moduli expressed as

$$\begin{aligned} \boldsymbol{C}^e &= (\kappa - 2\mu/3)\mathbf{I} \otimes \mathbf{I} - 2\mu\boldsymbol{I} \\ C_{ijkl} &= (\kappa - 2\mu/3)\delta_{ij}\delta_{kl} + \mu(\delta_{ik}\delta_{jl} + \delta_{il}\delta_{jk}) \end{aligned} \tag{7}$$

where $\mathbf{I}$ and $\boldsymbol{I}$ are the second and fourth rank unit tensors.

In the model described here, the associated plastic-flow rule without volumetric plastic strain is considered. That is, the direction of plastic flow coincides with the growth of yield surface,

$$\begin{aligned} &\boldsymbol{D}^p = \dot{\lambda}\boldsymbol{r}, \quad \boldsymbol{r} = \frac{3}{2\bar{\sigma}}\boldsymbol{\Sigma}^{\mathrm{dev}}, \\ &\boldsymbol{\Sigma}^{\mathrm{dev}} = \boldsymbol{\tau}^{\mathrm{dev}} - (1-\beta)\boldsymbol{\alpha}, \quad \bar{\boldsymbol{\sigma}} = \left(\frac{3}{2}\boldsymbol{\Sigma}^{\mathrm{dev}} : \boldsymbol{\Sigma}^{\mathrm{dev}}\right)^{\frac{1}{2}} \end{aligned} \tag{8}$$

As seen, the plastic flow includes an effective stress tensor $\boldsymbol{\Sigma}^{\mathrm{dev}}$ that contains the back stress tensor $\boldsymbol{\alpha}$ describing the effect of kinematic hardening, and an adjustable parameter $(1-\beta)$ describing the relative contribution of kinematic hardening in the overall behavior. Such an adjustable parameter has not been considered in other studies (White et al., 1990; Ekh et al., 2000; Pedersen, 2000) mentioned in the beginning. Then, the yield condition von Mises-type plasticity is expressed as

$$f = \bar{\sigma} - \sigma_y(\bar{\epsilon}) \tag{9}$$

where last term contains the initial yield stress (σ_0) and the isotopic hardening law. Thus, the plasticity model incorporates both kinematic and isotropic behavior. Their relative contribution is controlled by adjusting the parameter β. The kinematic hardening part is described by a generalized version of Armstrong–Frederick kinematic hardening rule (Kobayashi and Ohno, 2002):

$$\boldsymbol{\alpha} = \sum_{i=1}^{M} \boldsymbol{\alpha}^{(i)} \tag{10}$$

$$\overset{\nabla}{\boldsymbol{\alpha}}{}^{(i)} = \mu^{(i)}\boldsymbol{D}^p - \xi^{(i)}\dot{\lambda}\boldsymbol{\alpha}^{(i)} \tag{11}$$

while the isotropic hardening part is described by a model proposed by Kocks (1976),

$$\sigma_y(\bar{\epsilon}) = \sigma_0 + \beta Q(1 - \mathrm{e}^{-\gamma\bar{\epsilon}}) \tag{12}$$

where $\bar{\epsilon}$ is the equivalent plastic strain defined as $\int_0^t \dot{\lambda}\,\mathrm{d}t$.

The above equations together with the consistency condition $\dot{\lambda} \geqslant 0, f \leqslant 0, \dot{\lambda}f = 0$, can be used to obtain the plastic parameter $\dot{\lambda}$ and the elasto-plastic tangent moduli relating $\overset{\nabla}{\boldsymbol{\tau}} = \boldsymbol{C}^{\mathrm{ep}} : \boldsymbol{D}$,

$$\dot{\lambda} = \frac{\boldsymbol{C}^e : \boldsymbol{D}}{\sum_{i=1}^{M}\left(\frac{3}{2}\mu^{(i)} - \xi^{(i)}\boldsymbol{r} : \boldsymbol{\alpha}\right) + \mathrm{d}\sigma_y/\mathrm{d}\bar{\epsilon} + \boldsymbol{r} : \boldsymbol{C}^e : \boldsymbol{r}} \tag{13}$$

$$\boldsymbol{C}^{\mathrm{ep}} = \boldsymbol{C}^e - \frac{\boldsymbol{C}^e : \boldsymbol{r} \otimes \boldsymbol{r} : \boldsymbol{C}^e}{\sum_{i=1}^{M}(\frac{3}{2}\mu^{(i)} - \xi^{(i)}\boldsymbol{r} : \boldsymbol{\alpha}) + \mathrm{d}\sigma_y/\mathrm{d}\bar{\epsilon} + \boldsymbol{r} : \boldsymbol{C}^e : \boldsymbol{r}} \tag{14}$$

The above model has been implemented in a general purpose code ABAQUS through the user subroutine UMAT (HKS, 2002). In it, ABAQUS uses the Hughes–Winget incremental algorithm (Hughes and Winget, 1980) to handle the large deformation plasticity problem. More detailed explanations about the numerical implementation of the plasticity model are given in Appendix B.

2.2. Numerical model

In the following sections, the problem to be investigated is the indentation of elasto-plastic half space by a rigid spherical indenter of radius R (Fig. 1). In the contact region, the interaction between surfaces is considered to be frictionless. Two cases are considered, the first case refers to the monotonic loading, and the second one to cyclic loading. The first case is simply the first half cycle of the indentation curve while the second one involves loading–unloading for several cycles under constant or increasing maximum load in each cycle. Roles of yield stress and hardening parameters are studied in terms of the relation between Meyer hardness, which is defined as the normal indentation load divided by the projected contact area, $H = P/\pi a^2$, and indentation strain, a/R.

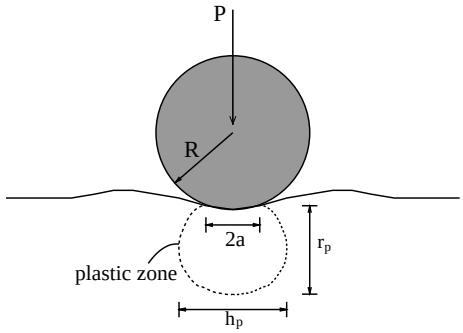

Fig. 1. Schematic of elasto-plastic indentation by a rigid sphere.

The elasto-plastic boundary value problem was solved using the finite element (FE) code ABAQUS. The FE model consists of a an axisymmetric mesh for the substrate which was made of 4-node linear elements, and a spherical rigid surface for the indenter. Only one half of the whole geometry is necessary. The sizes of the outer mesh boundaries were about 1000 times the largest contact radius. The preliminary calculation indicated that this was an adequate size for the problem. In the vicinity of the contact the mesh was made frier in order to produce accurate results.

3. Results for monotonic loading

3.1. Meyer hardness

The material inputs consist of two sets of stress–strain curves shown in Fig. 2. The two sets correspond to two different yield stress to modulus ratios (σ_{y0}/E). It is worth mentioning that effects of kinematic and isotropic hardening cannot be distinguished in the case of monotonic loading because proportional changes of stresses and strains occur. Thus, only the loading cycle (without unloading cycle) of the stress–strain curves are shown.

The theoretical basis of the problem is so far only available for the elastic case due to Hertz (Johnson, 1985). Meanwhile historically, the behavior involving elasto-plasticity has been treated in a more empirical manner by Tabor (1951) who used Meyer's definition of hardness (cited simply as hardness in this paper). By thoroughly analyzing the spherical indentation data, Tabor came up with a well known result $H = \mathrm{CF} \times \sigma_{y0}$. CF is generally known as the constraint factor whose value varies from 2.8 to 3.1 (Tabor, 1951; Ishlinsky, 1944; Richmond et al., 1974; Follansbee and Sinclair, 1984; Lee et al., 1972) if the substrate was rigid-perfectly plastic and from 1 to 3 if the substrate was elasto-plastic (Tabor, 1951; Tirupataiah and Sundararajan, 1991, 1987; O'Neill, 1967; Johnson, 1970, 1985). However, his finding is valid only beyond a certain indentation strain value. This is also what is shown in Fig. 3 which was obtained using inputs given in Fig. 1. The result was obtained from the FEM simulation by determining, at different load level, the contact radius of the solid indented by spheres whose radii varied between 300 and 1500 times the typical element size in the contact region. These radii were chosen so that the contact area was much larger than the typical element size. The contact radius was found accurately by examining the location only where the minimum normal pressure fell below 1% of the maximum value. Thus, the contact radius was not sampled at load levels where these locations were not well defined. Furthermore, to assure the accuracy large sphere radii were used for smaller loads, while at larger loads smaller spheres were used.

Tabor's equation has been argued to be valid only within the fully plastic range of the hardness curve. In Fig. 3, such an equation is seen only valid for the material without hardening (perfectly plastic) beyond a/R of about 50. To normalize the effect of hardening, it has been suggested (Tabor, 1951; Tirupataiah and Sundararajan, 1991, 1987) that the hardness be normalized by the yield stress corresponding to the plastic strain of $0.2a/R$. After performing such a procedure, the result is replotted in Figs. 4 and 5. Now, the normalized hardness relations for different materials appear to be tightly bound and hardly distinguishable from each

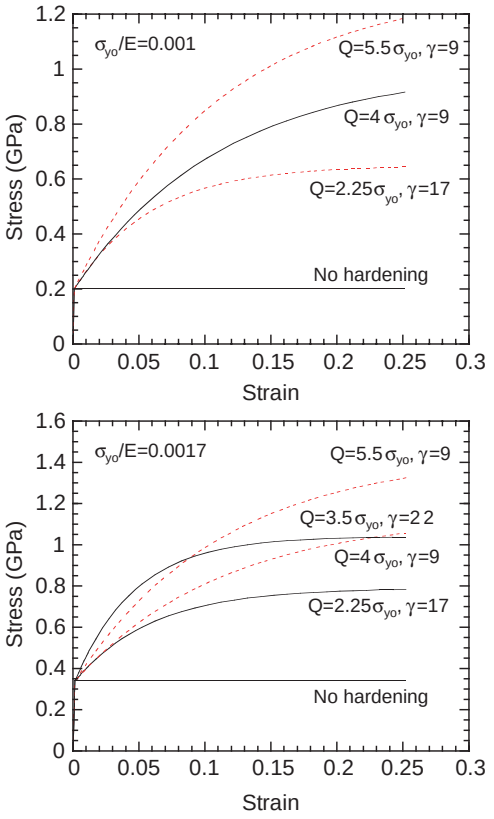

Fig. 2. Stress–strain curves for different hardening parameters.

other except for the material with $\gamma = 22$ (in Fig. 2). The curve from this material lies below the group of curves in Fig. 4. What separates this material is that the value of $0.2a/R$ used as the plastic strain is to high for such a material, a value of $0.16a/R$ will give a better result. A scatter band indicating the deviation of normalized hardness curves from the curve belonging to the perfectly plastic material can be seen in Fig. 6 which covers a wider range of material properties. From the above analysis we have found that the characterization of surface response through hardness vs. indentation strain can be sensitive to the choice of the multiplication factor in front of a/R.

There are basically three deformation regimes in the relation between the normalized hardness (Meyer hardness normalized by the yield strain obtain at equivalent strain of $0.2a/R$) and the normalized indentation strain ($aE/R\sigma_{yo}$): elastic, elastic–plastic, and fully plastic (Johnson, 1985). The elastic to elastic–plastic boundary is obtained from Hertz theory (Johnson, 1970, 1985),

$$p_o = \frac{3}{2}\frac{P}{\pi a^2} = \frac{3}{2}\bar{p} \tag{15}$$

where P and a are, respectively, the contact load and the contact radius. Yielding is determined using the von Mises criterion as follows:

$$\begin{aligned} \bar{\sigma}_{\max} &= \mathrm{Max}\sqrt{\frac{3}{2}[(\sigma_r - p_m)^2 + (\sigma_\theta - p_m)^2 + (\sigma_z - p_m)^2]} \\ p_m &= \frac{\sigma_r + \sigma_\theta + \sigma_z}{3} \end{aligned} \tag{16}$$

The stress components above refer to the subsurface stresses. They vary along the centerline of the contact loading as follows:

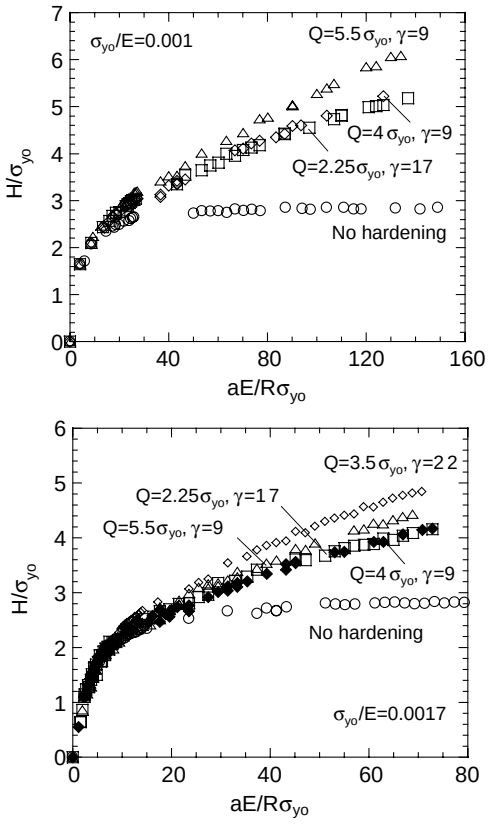

Fig. 3. Hardness curves for different hardening parameters.

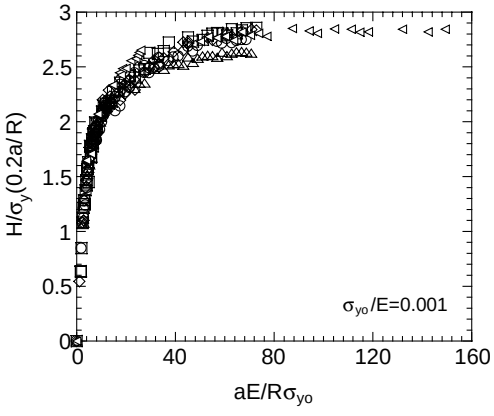

Fig. 4. Normalized hardness curves for different hardening parameters.

$$\frac{\sigma_r}{p_o}=\frac{\sigma_\theta}{p_o}=-(1-\nu)\left[1-\frac{z}{a}\tan^{-1}\left(\frac{a}{z}\right)\right]+\frac{1}{2(1+z^2/a^2)}$$
$$\frac{\sigma_z}{p_o}=-\frac{1}{1+z^2/a^2} \tag{17}$$

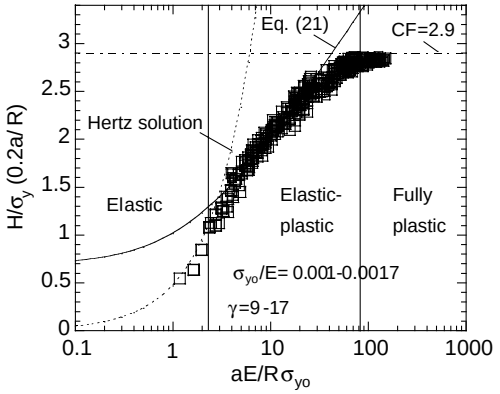

Fig. 5. Hardness curves of materials indicated in Fig. 2 except that having $\gamma = 22$, and their approximations for different deformation regimes.

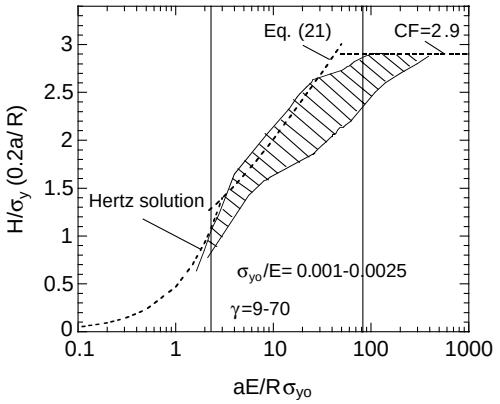

Fig. 6. Hardness curves of various materials and their approximations for different deformation regimes.

Thus, the condition at yield can be found,

$$\bar{\sigma}_{\max} = 0.93\bar{p} = \sigma_{\mathrm{yo}} \tag{18}$$

Notice that $\bar{p}$ is essentially the Meyer hardness (H) defined for the elastic range. At yield, the elastic limit in terms of H or $\bar{p}$ and a/R are

$$\bar{p} = \frac{4}{3\pi}\frac{E}{1-\nu^2}\left(\frac{a}{R}\right) = 1.08\sigma_{\mathrm{yo}}, \quad \frac{a}{R} = 0.81\pi(1-\nu^2)\frac{\sigma_{\mathrm{yo}}}{E} \tag{19}$$

Notice that in Figs. 4 and 5, hardness curves are similar to that of the perfectly plastic materials. This suggests that hardness can be approximated using analytical expressions defined in each deformation range. In the elastic range, Hertz solution is valid, in the elastic–plastic range an analytical expression can be found using the spherical cavity solution for perfectly plastic materials, and in the fully plastic range a constraint factor (CF) based on Tabor's empirical equation can be used. The Hertz solution has been given above and the constraint factor has been estimated to be 2.9. The spherical cavity solution is readily available for elastic-perfectly plastic materials, it describes the evolution of the plastic radius with contact radius (Johnson, 1970, 1985; Hill, 1950; Narasimhan, 2004):

$$\frac{\sigma_y}{E}\left[3(1-\nu)\frac{r_p^2}{a^2} - 2(1-2\nu)\frac{a}{r_p}\right]\frac{\mathrm{d}r_p}{\mathrm{d}a} = \frac{a}{2R} \tag{20}$$

The above equation can be solved analytically assuming $\mathrm{d}r_p/\mathrm{d}a = r_p/a$, as suggested in Johnson (1985), which gives

$$\frac{r_p}{a} = \left[\frac{\epsilon_o/2 + 2(1-2\nu)}{3(1-\nu)}\right]^{1/3}, \quad \epsilon_o = \frac{a/R}{\sigma_{yo}/E} \tag{21}$$

To calculate hardness, one first uses the relation between the size of plastic zone and the pressure ($\hat{p}$) applied inside a spherical cavity in an infinite medium given by Hill (1950). Then, based on the expression $\sigma_{zz} = \hat{p} + 2\sigma_y/3$ within the spherical cavity suggested by Johnson (1985) hardness is found to be

$$\begin{aligned} \hat{p} &= 2\sigma_y\left[\ln\left(\frac{r_p}{a}\right) + \frac{1}{3}\right] \\ H &= \hat{p} + \frac{2}{3}\sigma_y = 2\sigma_y\left[\ln\left(\frac{r_p}{a}\right) + \frac{2}{3}\right] \end{aligned} \tag{22}$$

It is worth mentioning that two recent papers by Park and Pharr (2004) and by Mesarovic and Fleck (1999) have looked also into the relation between and hardness and indentation strain. These two papers however, used different constitutive laws for the substrate. Yet, they found a quite similar hardness-indentation strain relation. Mesarovic and Fleck recognized that when the indentation strain exceeded some limit within the fully plastic zone hardness might not stay constant but decrease. We did not find this since we did not go beyond the limit described by Mesarovic and Fleck, which is primarily related to the geometric non-linearity. Park and Pharr who used the power law strain hardening, acknowledged this behavior as well and did not go beyond the aforementioned limit. They obtained, after normalizing hardness with yield stress at $0.2a/R$ (just like our approach), different hardness-indentation strain relations for different materials. In their work, the hardness relations seem to be spread due to differences in hardening exponent. This also what we found as shown in Fig. 6, but we also found that the spread was due to the factor 0.2 used in relating the indentation strain with the equivalent plastic strain, e.g. in H/σ_y ($0.2a/R$). If the factor was chosen appropriately, the spread disappears. In our case, the appropriate factor can vary from 0.15 to 0.25.

3.2. Plastic zone

To further see the role of plasticity it is necessary to observe the extent of the plastic deformation below the surface or the plastic zone. When the deformation is in the fully plastic regime, $H/\sigma_{yo} = \mathrm{CF} = \text{constant}$. This means, according to Eq. (21) above the plastic zone ratio r_p/a should also be constant. To obtain such a value we write

$$\frac{r_p}{a} = \exp\left(\frac{\mathrm{CF}}{2} - \frac{2}{3}\right) \tag{23}$$

The above equation is obtained from the cavity solution which implies the plastic zone shape to be spherical. The actual shape however, is not spherical and is shown schematically in Fig. 1. To characterize such a shape one can use the maximum depth or width of the plastic zone, r_p or h_p. When the maximum depth is used, its value normalized by the contact radius a (as suggested above) is plotted in Fig. 7 for materials defined by strain-curves in Fig. 2. For the perfectly plastic material, r_p/a appears to be close to the analytical estimate given above. For instance, for $\mathrm{CF} = 2.9$ a value of 2.2 is obtained for r_p/a. However, for different hardening materials r_p/a does not seem to be constant even for large indentation strains belonging to the fully plastic regime defined according to Figs. 4 and 5.

One apparent reason for such an increasing r_p/a is the lack of self-similarity in spherical indentation behavior. The other contributing factor is piling-up or sinking-in of the material at the free surface. In fact for hardening materials, simulation results indicate that the horizontal growth of the plastic zone as a function of a/R is not proportional to the vertical growth even in the so called fully plastic regime.

3.3. Relations between surface and subsurface strains

In the previous subsections, it has been shown that surface responses of different elasto-plastic materials can be normalized when expressed in terms of normalized hardness H/σ_y, and indentation strain $aE/R\sigma_{yo}$. As

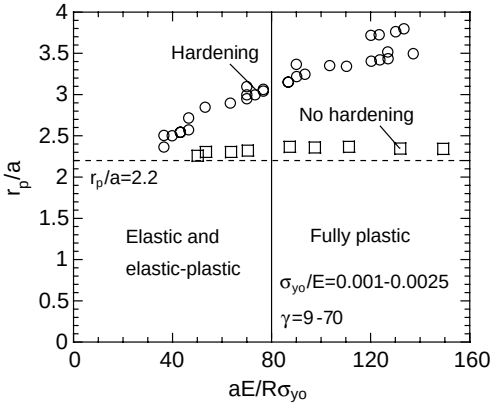

Fig. 7. Plastic zone size.

already shown, in the elastic–plastic deformation regime the plastic zone size is not scaled directly with the contact radius. The latter is supposed to represent the surface loading after being normalized by the indenter radius, a/R. Such an interpretation suggests that subsurface responses are more sensitive to plastic parameters, and their normalization or characterization, if possible, are not as easy as the surface response. To show this, the subsurface equivalent plastic strain will be compared for different materials.

The choice, the equivalent plastic strain, is obvious because it represents the plastic response. The location to be evaluated is chosen to be the point where yielding according to von Mises criterion first takes place. Our calculation indicated that the maximum von Mises stress which is also the first point to yield always occurs at the vertical axis of the indenter at the depth of $0.5a$ below the surface. The equivalent plastic strain at this point is simply:

$$\epsilon^*_{eq} = \lambda \quad (r = 0,\ z = 0.5a) \tag{24}$$

The result of plotting $\epsilon^*_{eq}E/\sigma_{yo}$ versus $aE/R\sigma_{yo}$ is shown in Fig. 8. There seems to be a unique relation between ϵ^*_{eq} and $aE/R\sigma_{yo}$ which is independent of plasticity parameters. This also suggests that ϵ^*_{eq} scales linearly with the indentation strain $aE/R\sigma_{yo}$ and thus, ϵ^*_{eq} can be a potential candidate to represent the subsurface plastic response. The scaling factor E/σ_{yo} appears to be a key parameter and cannot be simply cancelled out to preserve the relation shown in Fig. 8. The reason for this is because $\epsilon^*_{eq}E/\sigma_{yo}$ relates to $aE/R\sigma_{yo}$ according to a linear equation that has an offset when $aE/R\sigma_{yo} = 0$. Surely, ϵ^*_{eq} does not exist below the initial yield point and $\epsilon^*_{eq}E/\sigma_{yo} - aE/R\sigma_{yo}$ relation terminates at that point. Taking off E/σ_{yo} will produce several linear curves that have different offset values.

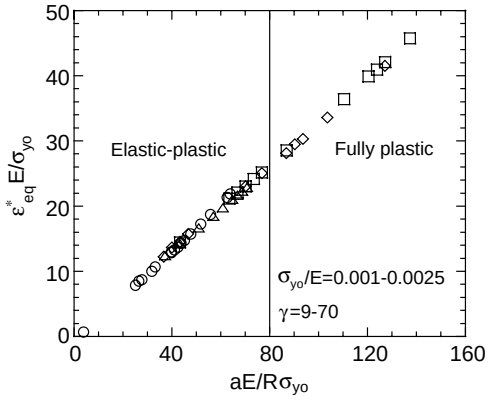

Fig. 8. Equivalent plastic strains for different materials at $r = 0$, $z = 0.5a$.

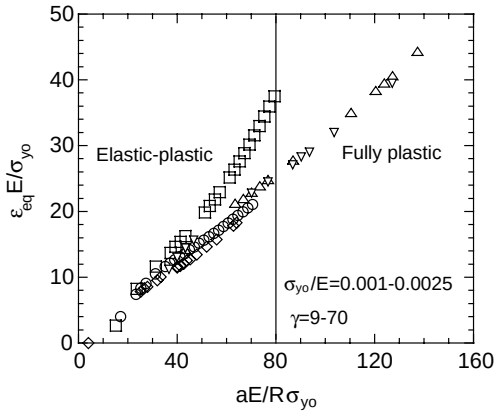

Fig. 9. Equivalent plastic strains for different materials at $r = 0$, $z = R/30$.

We have not been able to make the physical interpretation of ϵ^*_{eq} clearer since its location changes with a. Nevertheless, this finding implies that the plastic deformation at the location defined by a fixed ratio relative to the indentation radius scales uniquely with $aE/R\sigma_{yo}$. As a comparison, a plot of the variation of equivalent plastic strain at a fixed depth ($z = R/30$) with indentation strain is given in Fig. 9. A unique relation shown in Fig. 8 is not observed in this figure. Each relation basically depends on the set of material properties.

4. Results for non-monotonic loading

4.1. Load–displacements and surface profile

In this analysis, two cases of loading cycle shown in Fig. 10 are considered. They consist of indentation up to a maximum load and then reloading to zero. The first one (case A) corresponds to regular loading–unloading where the maximum load is kept constant every cycle. Meanwhile in the second one (case B), the maximum load in each cycle is increased 20% from the previous maximum. The material to be used for the simulation is described in Appendix A. Therein, a set of material parameters have been determined from the experimental data by Mizuno et al. (2000) and the effect of the plasticity parameter β has been presented. Evaluations of indentation strain and hardness were not attempted in this non-monotonic loading condition, primarily because they can not be easily interpreted when the surface has been repeatedly deformed and residual stresses exist beneath the surface.

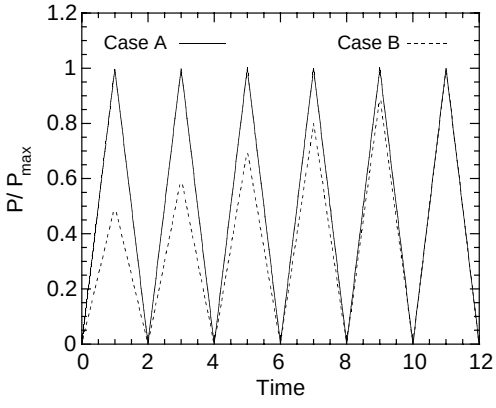

Fig. 10. Loading history.

Load–displacement curves for different combined hardening parameter β, including two extreme hardening materials, purely kinematic ($\beta = 0$) and purely isotropic ($\beta = 1$) hardening are plotted in Fig. 11 for the loading case A. The material with $\beta = 0.3$ is the simulated 316FR steel explained in Appendix A.

Notice that the load as well as the displacement have been normalized with their corresponding yield limits according to von Mises criterion (see also (19) above),

$$P_y = (1.08\pi)^3 \left[\frac{3\sigma_{yo}(1-\nu^2)}{4E}\right]^2 \sigma_{yo} R^2$$
$$\delta_y = \left[\frac{9P_y^2(1-\nu^2)^2}{16RE^2}\right]^{1/3} = \left[0.81\pi\sigma_{yo}\frac{(1-\nu^2)}{E}\right]^2 R \tag{25}$$

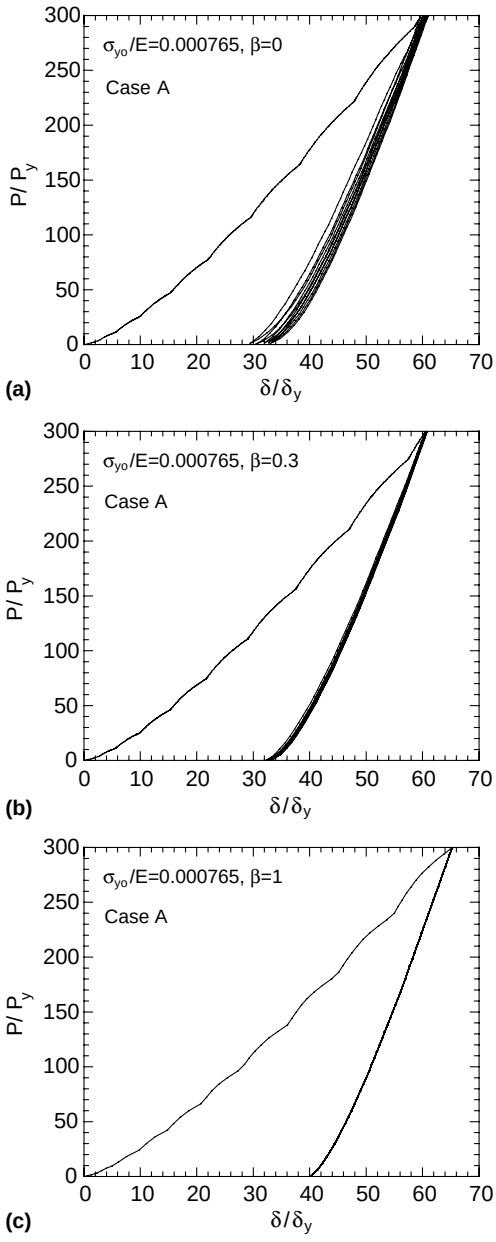

Fig. 11. Comparison of load–displacement curves for different combined hardening parameter β.

The most apparent influence of β can be seen by comparing the residual displacement cumulated over the cycle and the load–displacement loop. The accumulation of residual displacement seems to be higher for lower β implying the strong effect of kinematic hardening on the fatigue deformation. The accumulation appears to be minimum for larger β and no accumulation is found for the purely isotropic hardening material.

Results similar to above for the other loading case is shown in Fig. 12. Here, as before the kinematic hardening material exhibits some reverse plastic deformation. This can be seen from the loop formed during loading–unloading–reloading cycles which is a known artifact of Bauschinger effect. The two curves are also seen to strongly deviate from each other as the load increases.

The residual surface profile at the end of load cycles is shown in Fig. 13. Both profiles seem to show the pile-up behavior where the shoulder can be used to indicate the contact boundary. At some distance beyond the shoulder or the contact boundary both profiles appear to be very close to each other. Furthermore, the contact sizes of both judged from the shoulders are not so different. However, the profiles differ significantly inside the deformed contact region. The difference is most notable in the center displacement (x-coordinate is zero) as shown in Fig. 13, which can also be estimated from the difference in the residual depth of both curves in Fig. 12.

4.2. Stress, strain and residual plastic zone

Such a strong influence of β and the effect of load cycle can be observed in terms of Mises stress and equivalent plastic strain. In this study, the most significant plastic strain development has been observed at some

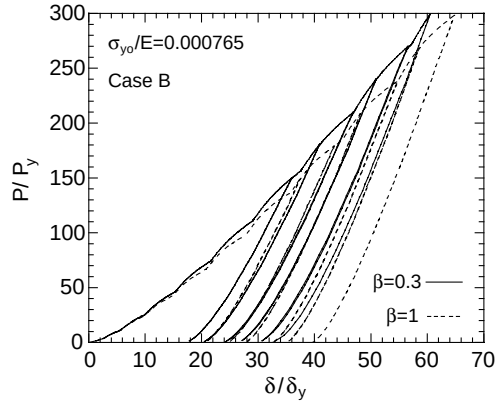

Fig. 12. Comparison of load–displacement curves for kinematic and isotropic hardening plasticity in case B.

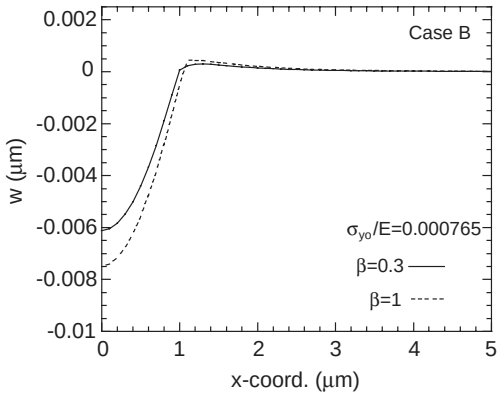

Fig. 13. Residual surface profile after the last cycle in case B.

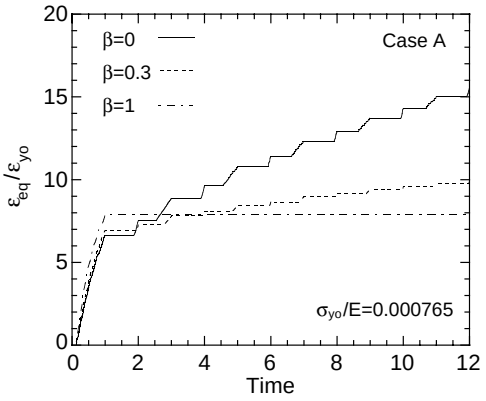

Fig. 14. Equivalent plastic strains for different combined hardening parameters β, case A.

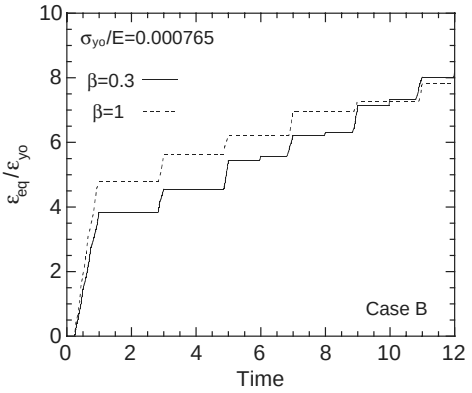

Fig. 15. Equivalent plastic strains for different combined hardening parameters β, case B.

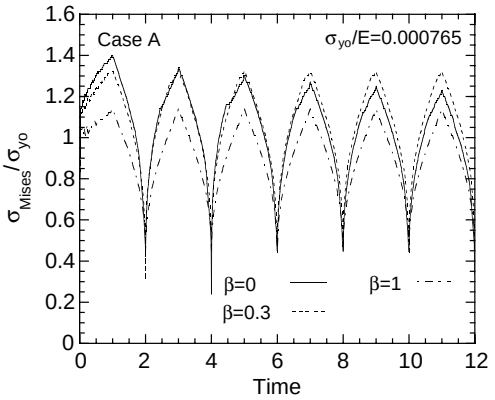

Fig. 16. Comparison of Mises stress for different combined hardening parameter β.

distance below the indentation center. The equivalent plastic strain development sampled at a distance of about $R/75$ under the indentation center is given Figs. 14 and 15. In both load cases, the materials dominated by kinematic hardening exhibit stronger plastic strain development. However, when the load case A is considered no equivalent plastic strain develops after the first loading cycle in the isotropic hardening material. This is also true for other locations in the substrate and explains why the indentation depth does not develop

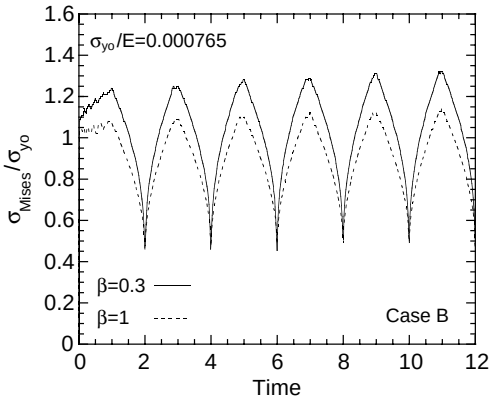

Fig. 17. Variation of Mises stresses just below the indenter tip for different hardening behavior.

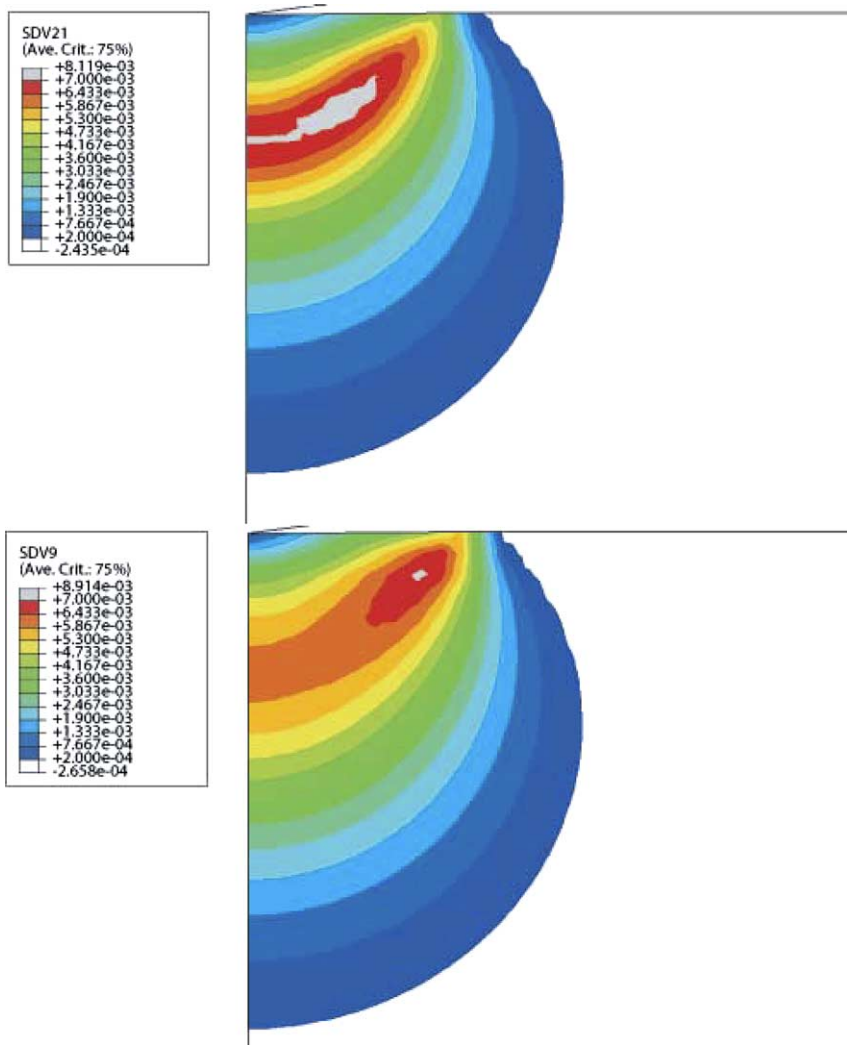

Fig. 18. Contours of residual equivalent plastic strain for $\beta = 0.3$ (top) and $\beta = 1$ (bottom) in case B.

further after the first cycle. The different trend between the kinematic and isotropic hardening can be attributed to the fact that the yield stress during cyclic loading changes significantly in the kinematic hardening but not in the isotropic hardening. Furthermore, at the location sampled, the plastic strain does not seem to be reversed. At some other locations however, the plastic strain does reverse during unloading of materials with lower β. This is true since we found that contours of equivalent plastic strain at the maximum load, was slightly different compared to that at zero load (residual).

Variations of Mises stress with time, sampled from the element directly under the indenter tip is shown in Fig. 16 for case A and Fig. 17 for case B. Both cases suggest that there is a significant stress relaxation in materials with low β or the materials exhibiting strong kinematic hardening behavior. Notice that in the first cycle the stress variations in different materials are almost the same. After the first cycle, the reduction of Mises stress in kinematic hardening materials together with the occurrence of cumulative residual displacement (in Figs. 11 and 12) also suggest that reverse plasticity may take place. This means that in materials dominated by kinematic hardening yielding can also occur during unloading, just as we have stated for the case of plastic strain variation at the end of the previous paragraph. This indicates that the typical one-cycle indentation test may not be sufficient to characterize the effect of plastic behavior.

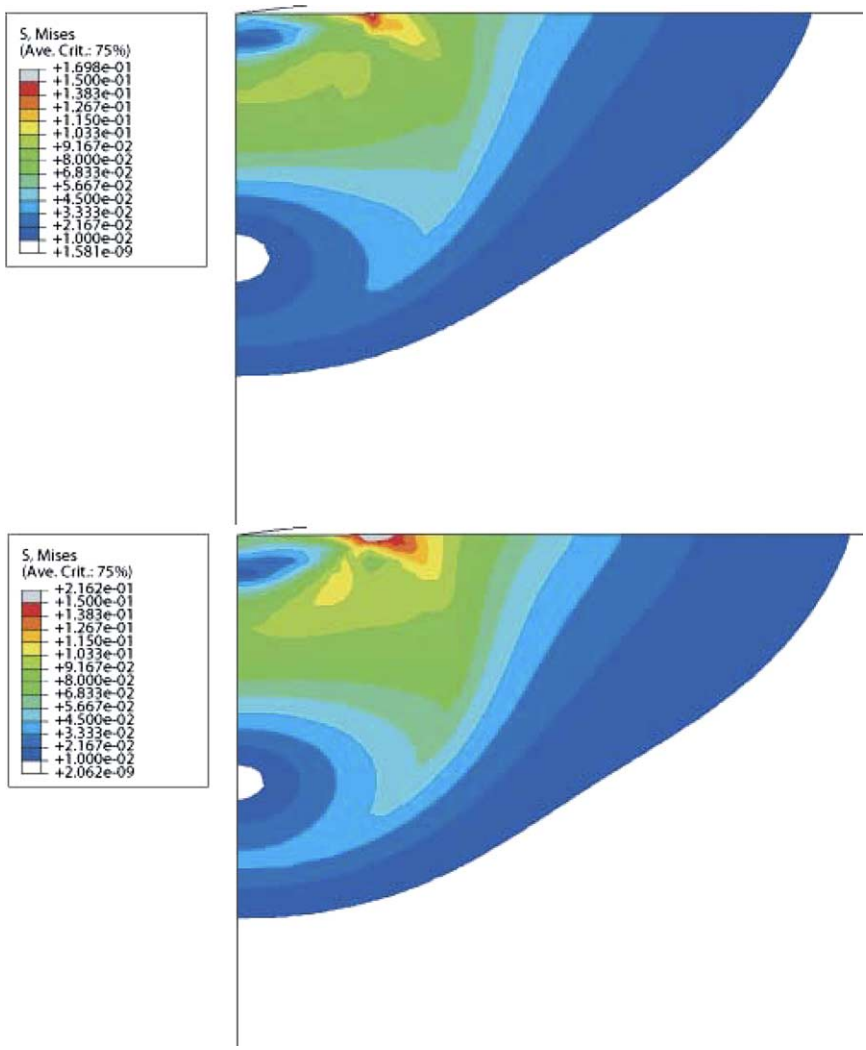

Fig. 19. Contours of residual Mises stress for $\beta = 0.3$ (top) and $\beta = 1$ (bottom) in case B.

The equivalent plastic strain contours are shown in Fig. 18 only for the load case B. These contours, as well as the other contours latter, depict the condition at the end of the loading cycle (residual state) and are shown axisymmetrically with loading directed in the vertical direction. Furthermore, the top contour corresponds to the simulated 316FR steel and the bottom one to the purely isotropic ($\beta = 1$) hardening. As seen from the legends, both contours exhibit similar magnitudes of maximum plastic strains. However, the simulated 316FR steel (top) gives a wider area of maximum plastic strain (grey color) compared to the isotropic hardening material (bottom). Meanwhile, the size of the plastic zone for a minimum plastic strain of around 0.0002 are pretty much the same for both materials. Notice, that the maximum and minimum limits of the scale used for both contours have been set the same. The contours of Mises stress are given in Fig. 19, where the stress distributions appear to be quite different in the two materials. The maximum Mises stress is also found to be higher in the isotropic hardening material but not directly below the center of indenter, where Mises stress from Fig. 17 is seen higher in the simulated 316FR steel. Somewhere below the indentation center both materials seem to experience negligible von Mises stress indicated by the white regions. Around these regions von Mises stress is still comparable to the material yield stress (0.15 GPa). It is possible that therein the stress state is close to purely hydrostatic with very small deviatoric stresses. It must be understood that the contours correspond to the unloaded state where the above behavior may occur due to the residual plastic behavior.

5. Conclusions

The results from monotonic loading reveal that stress–strain curves of materials can, up to a certain degree, be described by hardness-indentation strain relations or vice versa. This is true because the normalization of hardness by yield stress at a certain characteristic indentation strain ($\chi \times a/R$) seems to bring different hardness curves into almost a single curve. However, due to different hardening rate, yield stress, and χ these different hardness curves, after being normalized, do not merge into a single curve corresponding to the hardness curve of perfectly plastic materials. Instead, the normalized hardness curves form a scatter band. To minimize such a scatter appropriate value of χ must be chosen for different materials. Notably, for most materials investigated $\chi = 0.2$ is appropriate but for high hardening materials (high γ) χ varies between 0.15 and 0.25.

It is worth mentioning that difficulties in measuring the contact radius may also hinder us from obtaining accurate hardness-indentation strain relations. When such relations can be accurately obtained however, normalization of them by suitably chosen indentation strains can produce a relatively uniform hardness curve general enough for different plasticity parameters. The normalized curves, being similar to the hardness curve of perfectly plastic materials, can be fitted analytically using the Hertz solution and the spherical cavity solution. The latter should be considered as an approximation since it does not intersect the Hertz solution at the initial yield point but slightly higher. This deviation can be considered minor as seen from how well the cavity solution matches the numerical result in Fig. 5. Furthermore, assuming a hardening material follows such an analytical form and its hardness curve in the form of Fig. 3 is available, one can backcalculate the yield stress corresponding to yield strain of $0.2a/R$ or constant $\times\, 0.2a/R$.

In general, the plastic zone size and its shape in the fully plastic region appear to be dependent on the plasticity parameters. In this region, the spread of plastic zone occurs more towards the free surface, making the plastic zone's depth to contact radius ratio vary. This is not the case for the material without hardening, where the plastic zone's depth to contact radius ratio stays relatively constant.

In order to be able to compare isotropic and pure kinematic hardening behavior, it is necessary to consider cyclic loading. The difference between the two hardening laws cannot be easily distinguished from the cyclic indentation load–displacement curves and is difficult to see in terms of deformed surface profile. In general, materials with the kinematic or combined hardening laws exhibit some form of reversible plastic deformation which can be identified from the loop formed during the load–unload–reload cycle.

Differences in terms of residual equivalent plastic strain, Mises stress, and their variations with displacement/load cycles are quite obvious. This and the above findings suggest that we have to look carefully for what happens below the surface (subsurface response) in studying the role of plasticity on indented materials. The surface response alone is not sufficient to describe or to imply the critical conditions of subsurface deformation. In addition, applications involving cyclic mechanical contact requires good knowledge of the materials in contact. A kinematic or combined hardening law is more appropriate for materials exhibiting Bauschinger

effect. As suggested by presented results, its use can lead to a tremendous increase of subsurface's equivalent plastic strain while von Mises stress is lowered considerably.

Appendix A. Plasticity parameters

The parameters used for simulating the cyclic indentation are similar to the set given here. The parametric study is done by fixing the aforementioned set and varying the parameter β.

The present plasticity model is also capable of modeling the cyclic stress–strain response of a real material. As an example, the cyclic tension test data of 316FR steel at room temperature given in (Mizuno et al., 2000) has been simulated. For the strain history shown in Fig. A.1 the experimental stress–strain response looks like that in Fig. A.2(a) and the prediction is shown in Fig. A.2(b). It must be understood that this study does not try to find the algorithm to backcalculate the model parameters so the fitting to the experimental data was a

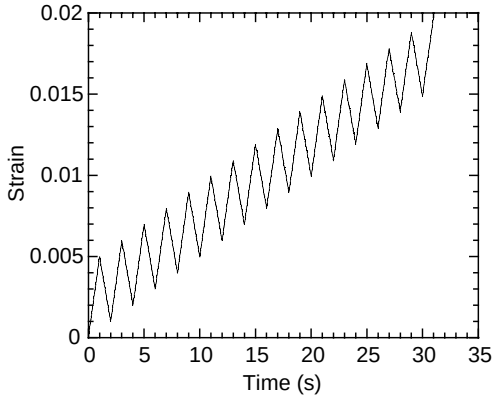

Fig. A.1. Strain history used to generate the experimental data in Mizuno et al. (2000).

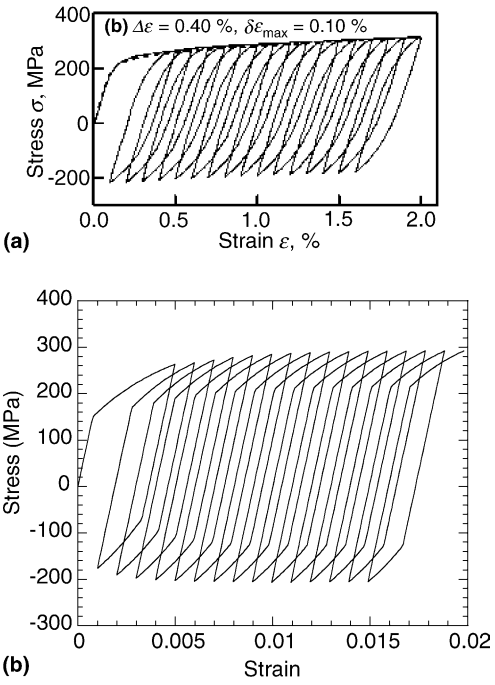

Fig. A.2. Experimental data in Mizuno et al. (2000) (a) and the model prediction (b).

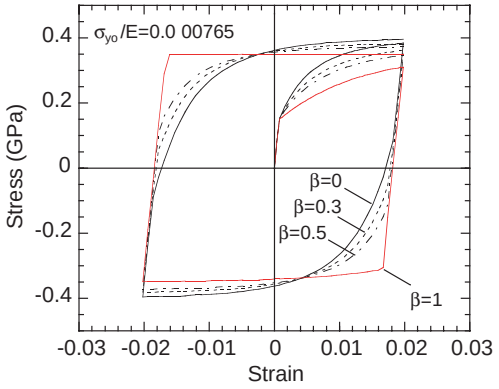

Fig. A.3. Influence of β on the uniaxial stress–strain curve.

trial and error process rather than using inverse or optimization algorithms. Yet, comparing Figs. A.2a and b the prediction appears to be reasonably good. The model parameters used for the prediction are the following: $E = 196$ GPa, $v = 0.3$, $\beta = 0.3$, $\sigma_o = 0.15$ GPa, $Q = 0.2$ GPa, $\gamma = 90$, $\mu^{(1)} = 12$ GPa, $\xi^{(1)} = 220$, $\mu^{(2)} = 26$ GPa, $\xi^{(2)} = 540$, $\mu^{(3)} = 7$ GPa, $\xi^{(3)} = 110$. One can certainly improve this by adding more parameters and applying some optimization algorithms to find the model parameters that give the best fit to the data.

One of the important parameters in the present model is the mixed hardening parameter β. The purely kinematic hardening behavior is achieved using $\beta = 0$ while the purely isotropic one is obtained using $\beta = 1$. Using the same material parameters presented before, the effect of varying β on the stress–strain cycle can be seen in Fig. A.3. It clear from the figure that β changes the hardening rate as well as the saturation yield stress. For purely isotropic hardening, the latter is Q in Eq. (12). Meanwhile purely kinematic hardening, it is a function of $\mu^{(i)}$ and $\xi^{(i)}$.

We would like to note here that the present model coincides with the Chaboche model in ABAQUS when $\mu^{(i)}$ and $\xi^{(i)}$ are limited to the first term. The mixed hardening parameter (β) can also be incorporated into the parameters in Chaboche model. In fact, the present model has been verified by Chaboche model and the results of both models appeared to be similar. When one uses Chaboche model for the monotonic loading, the stress–strain curve increases proportionally and Kock's model for isotropic hardening and Armstrong–Frederick kinematic hardening model will coincide with each other.

Appendix B. Numerical implementation

The integration of the above constitutive law was carried out using the backward Euler method with the closest point projection algorithm. For the small deformation problem it follows closely the scheme detailed by Kobayashi and Ohno (2002). In ABAQUS, we extend the method to handle the large deformation problem using the Hughes–Winget incrementally objective integration scheme and approximate the Kirchoff stress tensor as the Cauchy stress tensor ($\boldsymbol{\tau} \approx \sigma$). The latter is a valid approximation as long as the volumetric deformation involved is small. Such a case certainly holds for elastic–plastic deformation behavior of most metals, which are the focus of this study, where the elastic strains are small compared to their plastic counterpart and the volumetric plastic strain is negligible. Detailed discussions on the implementation of the Hughes–Winget integration scheme can be found in (Fish and Shek, 1999) and references quoted therein.

For the time increment n to $n+1$, the symmetric part of the velocity gradient is

$$\boldsymbol{D} = \mathrm{sym}\left(\frac{\partial \boldsymbol{v}}{\partial \boldsymbol{x}}\right) \tag{B.1}$$

$$\boldsymbol{D}_{n+1} = \boldsymbol{D}^e_{n+1} + \boldsymbol{D}^p_{n+1} \tag{B.2}$$

In the beginning of each increment, the elastic and plastic strain components are rotated according to:

$$\begin{aligned} \boldsymbol{E}^e_{n+1} &= \Delta\boldsymbol{R}^{\mathrm{T}} \cdot \boldsymbol{E}^e_n \cdot \Delta\boldsymbol{R} + \boldsymbol{D}^e_{n+1}\Delta t = \Delta\boldsymbol{R}^{\mathrm{T}} \cdot \boldsymbol{E}^e_n \cdot \Delta\boldsymbol{R} + \Delta\boldsymbol{E}^e_{n+1} \\ \boldsymbol{E}^p_{n+1} &= \Delta\boldsymbol{R}^{\mathrm{T}} \cdot \boldsymbol{E}^p_n \cdot \Delta\boldsymbol{R} + \boldsymbol{D}^p_{n+1}\Delta t = \Delta\boldsymbol{R}^{\mathrm{T}} \cdot \boldsymbol{E}^p_n \cdot \Delta\boldsymbol{R} + \Delta\boldsymbol{E}^p_{n+1} \end{aligned} \tag{B.3}$$

with the increment of rotation given by:

$$\Delta \boldsymbol{R} = \left(\boldsymbol{I} - \frac{1}{2}\Delta \boldsymbol{W}\right)^{(-1)} \cdot \left(\boldsymbol{I} + \frac{1}{2}\Delta \boldsymbol{W}\right)$$
$$\Delta \boldsymbol{W} = \operatorname{asym}\left(\frac{\partial \Delta \boldsymbol{u}}{\partial \boldsymbol{x}_{n+1/2}}\right) \tag{B.4}$$

Furthermore, the following approximation is also made to Eq. (5):

$$\begin{aligned}\sigma_{n+1} &\approx \Delta \boldsymbol{R}^{\mathrm{T}} \cdot \sigma_n \cdot \Delta \boldsymbol{R} + \Delta \sigma_{n+1} \\ &= \Delta \boldsymbol{R}^{\mathrm{T}} \cdot \sigma_n \cdot \Delta \boldsymbol{R} + \boldsymbol{C}^e \cdot (\Delta \boldsymbol{E}_{n+1} - \Delta \boldsymbol{E}^p_{n+1})\end{aligned} \tag{B.5}$$

$$\Delta \boldsymbol{E}^p_{n+1} = \Delta \lambda_{n+1} \boldsymbol{r}_{n+1} \tag{B.6}$$

$$\boldsymbol{r}_{n+1} = \frac{3[\boldsymbol{s}_{n+1} - (1-\beta)\boldsymbol{\alpha}_{n+1}]}{2\bar{\sigma}_{n+1}} \tag{B.7}$$

In the above equation, $\boldsymbol{s}$ is the deviatoric part of $\boldsymbol{\sigma}$ and $\Delta\lambda$ is the magnitude of the plastic strain increment. All other parameters and variables are as explained in the text. The evolution of the back stress tensor follows the same integration scheme as the stress tensor,

$$\boldsymbol{\alpha}_{n+1} = \sum_{i=1}^{M} \boldsymbol{\alpha}^{(i)}_{n+1} \tag{B.8}$$

$$\boldsymbol{\alpha}^{(i)}_{n+1} = \Delta \boldsymbol{R}^{\mathrm{T}} \cdot \boldsymbol{\alpha}^{(i)}_n \cdot \Delta \boldsymbol{R} + (\mu^{(i)} \boldsymbol{r}_{n+1} - \xi^{(i)} \boldsymbol{\alpha}^{(i)}_{n+1}) \Delta \lambda_{n+1} \tag{B.9}$$

Collecting the terms containing the current value of the back stress tensor gives

$$\boldsymbol{\alpha}^{(i)}_{n+1} = \frac{\Delta \boldsymbol{R}^{\mathrm{T}} \cdot \boldsymbol{\alpha}^{(i)}_n \cdot \Delta \boldsymbol{R} + \mu^{(i)} \Delta \lambda_{n+1} \boldsymbol{r}_{n+1}}{1 + \xi^{(i)} \Delta \lambda_{n+1}} \tag{B.10}$$

Next, we implement the closest point projection or the radial mapping algorithm. The initial guess for the stress tensor as the elastic predictor is

$$\boldsymbol{\sigma}^*_{n+1} = \Delta \boldsymbol{R}^{\mathrm{T}} \cdot \boldsymbol{\sigma}_n \cdot \Delta \boldsymbol{R} + \boldsymbol{C}^e \cdot \Delta \boldsymbol{E}_{n+1} \tag{B.11}$$

The yield condition is checked using

$$f^*_{n+1} = \frac{3}{2}[\boldsymbol{s}^*_{n+1} - (1-\beta)\boldsymbol{\alpha}_{n+1}] : [\boldsymbol{s}^*_{n+1} - (1-\beta)\boldsymbol{\alpha}_{n+1}] - \sigma_{y_{n+1}} \tag{B.12}$$

When $f^*_{n+1} < 0$ then $\boldsymbol{\sigma}^*_{n+1}$ is taken as the correct guess giving $\boldsymbol{\sigma}_{n+1}$. If $f^*_{n+1} \geqslant 0, \boldsymbol{\sigma}_{n+1}$ is corrected using the plastic corrector

$$\boldsymbol{\sigma}_{n+1} = \boldsymbol{\sigma}^*_{n+1} - \boldsymbol{C}^e \cdot \Delta \boldsymbol{E}^p_{n+1} = \boldsymbol{\sigma}^*_{n+1} - \Delta \boldsymbol{\lambda}_{n+1} \boldsymbol{C}^e \cdot \boldsymbol{r}_{n+1} \tag{B.13}$$

For isotropic elastic materials with incompressible plasticity, the above equation leads to

$$\begin{aligned}s_{n+1} - (1-\beta)\boldsymbol{\alpha}_{n+1} &= s^*_{n+1} - 2G\Delta\lambda_{n+1}\boldsymbol{r}_{n+1} - (1-\beta)\sum_{i=1}^{M} \frac{\Delta \boldsymbol{R}^{\mathrm{T}} \cdot \boldsymbol{\alpha}^{(i)}_n \cdot \Delta \boldsymbol{R} + \mu^{(i)} \Delta \lambda_{n+1} \boldsymbol{r}_{n+1}}{1 + \xi^{(i)} \Delta \lambda_{n+1}} \\ &= \sigma_{y_{n+1}} \left[\boldsymbol{s}^*_{n+1} - (1-\beta)\sum_{i=1}^{M} \frac{\Delta \boldsymbol{R}^{\mathrm{T}} \cdot \boldsymbol{\alpha}^{(i)}_n \cdot \Delta \boldsymbol{R}}{1 + \xi^{(i)} \Delta \lambda_{n+1}}\right] \\ &\quad \times \left[\sigma_{y_{n+1}} + \frac{3}{2}\Delta\lambda_{n+1}\left((1-\beta)\sum_{i=1}^{M} \frac{\mu^{(i)}}{1 + \xi^{(i)} \Delta \lambda_{n+1}} + 2G\right)\right]^{-1}\end{aligned} \tag{B.14}$$

Thus, when $\Delta\lambda_{n+1}$ has been found, (B.14) updates the deviatoric stress from its initial guess. By applying the yield condition, a non-linear scalar equation of the following is obtained

$$\begin{aligned}
\Delta\lambda_{n+1} &= \frac{\sqrt{\frac{3}{2}(\boldsymbol{s}^*_{n+1}-\bar{\boldsymbol{\alpha}}_n):(\boldsymbol{s}^*_{n+1}-\bar{\boldsymbol{\alpha}}_n)}-\sigma_{y_{n+1}}}{\frac{3}{2}(1-\beta)B_{n+1}+3G}\\
\bar{\boldsymbol{\alpha}}_n &= (1-\beta)\sum_{i=1}^{M}\frac{\Delta\boldsymbol{R}^{\mathrm{T}}\cdot\boldsymbol{\alpha}^{(i)}_n\cdot\Delta\boldsymbol{R}}{1+\xi^{(i)}\Delta\lambda_{n+1}}\\
B_{n+1} &= \sum_{i=1}^{M}\frac{\mu^{(i)}}{1+\xi^{(i)}\Delta\lambda_{n+1}}
\end{aligned} \tag{B.15}$$

The above equation is a non-linear scalar equation to be solved by an iteration procedure. Kobayashi and Ohno (2002) and Ohno and Abdel-Karim (2000) suggested a successive substitution scheme. We have solved this using both the successive substitution and Newton methods. For the uniaxial tension of an eight-node 3-D element used to produce Fig. A.1, the solution by the Newton method was as a accurate as that obtained using the successive substitution scheme, but it needed a little less iteration. In the implementation of the Newton method, the necessary first order derivative of the residual was found analytically for all terms except for the term containing $\boldsymbol{s}^*$ which was found numerically. For the calculation given previously, the number of iterations (k) averaged over all integration points in an element was less than six for the tolerance of $|(\Delta\lambda^{k+1}_{n+1}-\Delta\lambda^{k}_{n+1})/\sigma_o| \leqslant 10^{-6}$. The elasto-plastic tangent moduli has been obtained using a general form derived by Kobayashi and Ohno (2002), which can be written as

$$\frac{\mathrm{d}\Delta\boldsymbol{\sigma}_{n+1}}{\mathrm{d}\Delta\boldsymbol{D}_{n+1}} = \boldsymbol{C}^e - 4G^2\boldsymbol{M}^{-1}_{n+1}\cdot\boldsymbol{I}^{\mathrm{dev}} \tag{B.16}$$

where $\boldsymbol{C}^e$ is the elastic moduli, $\boldsymbol{I}^{\mathrm{dev}} = \boldsymbol{I}-(\mathbf{I}\otimes\mathbf{I})/3$, and $\boldsymbol{M}_{n+1}$ is defined as

$$\boldsymbol{M}_{n+1} = 2G\boldsymbol{I} + (1-\beta)\boldsymbol{H}_{n+1} + \frac{\mathrm{d}\sigma_y}{\mathrm{d}\bar{\epsilon}_{n+1}}\boldsymbol{r}_{n+1}\otimes\boldsymbol{r}_{n+1} + \frac{\sigma_{y_{n+1}}}{\Delta\lambda_{n+1}}\times\left(\boldsymbol{I}-\frac{2}{3}\boldsymbol{r}_{n+1}\otimes\boldsymbol{r}_{n+1}\right) \tag{B.17}$$

where $\bar{\epsilon} = \int_0^t d\lambda$ and

$$\boldsymbol{H}_{n+1} = \frac{\mathrm{d}\Delta\boldsymbol{\alpha}_{n+1}}{\mathrm{d}\Delta\boldsymbol{D}^p_{n+1}} = \sum_{i=1}^{M}\boldsymbol{H}^{(i)}_{n+1} \tag{B.18}$$

$$\boldsymbol{H}^{(i)}_{n+1} = \left(\mu^{(i)}\boldsymbol{I}-\frac{2}{3}\xi^{(i)}\boldsymbol{\alpha}_{n+1}\otimes\boldsymbol{r}_{n+1}\right)\Big/\left(1+\xi^{(i)}\Delta\lambda_{n+1}\right) \tag{B.19}$$

We report here that the result obtained using the above implementation can be checked with that obtained using the large-deformation plasticity option in ABAQUS. In particular, for the monotonic loading using a tabulated values of true plastic stress–strain relation and for the cyclic loading using the combined hardening option (Chaboche model) the results of the present implementation and built-in ABAQUS models are similar. In the case of the cyclic loading using the combined hardening option in ABAQUS (Chaboche model), the same result as that of the present model can be obtained if $\mu^{(i)}$ and $\xi^{(i)}$ are limited to one term. It is also true for any value of β because it can be embedded in the combined hardening parameters of ABAQUS. Such a finding basically confirms the accuracy of the integration algorithm.

References

Armstrong, P.J., Frederick, C.O., 1966. A mathematical representation of the multiaxial Bauschinger effect. CEGB Report RD/B/N731, Berkley Nuclear Lab., Berkley, UK.

Belytschko, T., Liu, W.K., Moran, B., 2001. Nonlinear Finite Elements for Continua and Structures. John Wiley, Chichester.

Bhattacharya, A.K., Nix, W.D., 1988. Finite element simulation of indentation experiments. Int. J. Solids Struct. 24, 881–991.

Bower, A.F., 1989. Cyclic hardening properties of hard-drawn copper and rail steel. J. Mech. Phys. Solids 37, 455–470.

Bucaille, J.L., Stauss, S., Felder, E., Michler, J., 2003. Determination of plastic properties of metals by instrumented indentation using different sharp indenters. Acta Mater. 6, 1663–1678.

Dao, M., Chollacoop, N., Van Vliet, K.J., Venkatesh, T.A., Suresh, S., 2001. Computational modeling of the forward and reverse problems in instrumented sharp indentation. Acta Mater. 49, 3899–3918.

Ekh, M., Johansson, A., Thorberntson, H., Josefson, B.F., 2000. Models for cyclic ratchetting plasticity-integration and calibration. J. Eng. Mater. Technol. 122, 49–55.

Fish, J., Shek, K., 1999. Computational aspect of incrementally objective algorithm for large deformation plasticity. Int. J. Numer. Methods Eng. 44, 839–851.

Follansbee, P.S., Sinclair, G.B., 1984. Quasi static normal indentation of an elasto-plastic half-space by a rigid sphere-I: analysis. Int. J. Solids Struct. 20, 81–91.

Hardy, C., Baronet, C.N., Tordion, G.V., 1971. Elastoplastic indentation of a half-space by a rigid sphere. J. Numer. Meth. Eng. 3, 451–466.

Hibbitt, Karlsson, Sorensen (HKS), Inc., 2002. ABAQUS Version 6.3 User's Manual. HKS Inc.

Hill, R., 1950. The Mathematical Theory of Plasticity. Clanderon Press, Oxford.

Huber, N., Tsakmakis, Ch., 1998. Experimental and theoretical investigations of the effect of kinematic hardening on spherical indentation. Mech. Mater. 27, 241–248.

Huber, N., Tsakmakis, Ch., 1999a. Determination of constitutive properties from spherical indentation data using neural networks-I: the case of pure kinematic hardening in plasticity laws. J. Mech. Phys. Sol. 47, 1569–1588.

Huber, N., Tsakmakis, Ch., 1999b. Determination of constitutive properties from spherical indentation data using neural networks-I: plasticity with nonlinear isotropic and kinematic hardening in plasticity laws. J. Mech. Phys. Sol. 47, 1589–1607.

Hughes, T.J.R., Winget, J., 1980. Finite rotation effects in numerical integration of rate constitutive equations arising in large deformation analysis. Int. J. Numer. Meth. Eng. 15, 1862–1867.

Ishlinsky, A.I., 1944. The axi-symmetrical problem in plasticity and the Brinell test. J. Appl. Math. Mech. (USSR) 8, 201.

Jayaraman, S., Hahn, G.T., Oliver, W.C., Rubin, C.A., Batias, P.C., 1998. Determination of monotonic stress–strain curve of hard materials from ultra-low-load indentation tests. Int. J. Solids Struct. 35, 365–381.

Jiang, Y., Sehitoglu, H., 1996. Rolling contact stress analysis with the application of a new plasticity model. Wear 191, 35–44.

Jiang, Y., Sehitoglu, H., 1996a. Modelling of cyclic ratchetting plasticity, part I: development of constitutive relations. J. Appl. Mech. 63, 726–733.

Jiang, Y., Sehitoglu, H., 1996b. Modelling of cyclic ratchetting plasticity, part II: comparison of model simulations with experiments. J. Appl. Mech. 63, 726–733.

Johnson, K.L., 1970. The correlation of indentation experiment. J. Mech. Phys. Solids 18, 115–126.

Johnson, K.L., 1985. Contact Mechanics. Cambridge University Press, Cambridge.

Kobayashi, M., Ohno, N., 2002. Int. J. Numer. Method Eng. 53, 2217.

Kocks, U.F., 1976. Laws for work-hardening and low-temperature creep. J. Eng. Mater. Technol. 98, 76–85.

Koeppel, B.J., Subhash, G., 1999. Characteristics of residual plastic zone under static and dynamic Vickers indentations. Wear 224, 56–67.

Kral, E.R., Komvopoulos, K., Bogy, D.B., 1993. Elastic-plastic finite element analysis of repeated indentation of a half-space by a rigid sphere. J. Appl. Mech. 60, 829–841.

Lee, C.H., Masaki, S., Kobayashi, S., 1972. Analysis of ball indentation. Int. J. Mech. Sci. 14, 417–426.

Mesarovic, S.D., Fleck, N.A., 1999. Spherical indentation of elastic–plastic solids. Proc. R. Soc. Lond. A 455, 2707–2728.

Meyer, E., 1908. Zeits. d. Vereiness Deutsch. Ing., p. 52.

Mizuno, M., Mima, Y., Abdel-Karim, M., Ohno, N., 2000. Uniaxial ratchetting of 316FR steel at room temperature, part I: experiment. J. Eng. Mater. Technol. 122, 29–34.

Narasimhan, R., 2004. Analysis of indentation of pressure sensitive plastic solids using the expanding cavity model. Mech. Mater. 36, 633–645.

Ohno, N., Abdel-Karim, M., 2000. Uniaxial ratchetting of 316FR steel at room temperature, part II: constitutive modeling and simulation. J. Eng. Mater. Technol. 122, 35–41.

O'Neill, H., 1967. The Hardness of Metals and Alloys. Chapman and Hall, London.

Park, Y.J., Pharr, G.M., 2004. Nanoindentation with spherical indenters: finite element studies of deformation in the elastic–plastic regime. Thin Solid Films 447–448, 246–250.

Pedersen, T.O., 2000. Numerical modelling of cyclic plasticity and fatigue damage in cold-forging tools. Int. J. Mech. Sci. 42, 799–818.

Richmond, O., Morrison, H.L., Devenpeck, M.L., 1974. Sphere indentation with application to the Brinell hardness test. Int. J. Mech. Sci. 16, 75–82.

Samuels, L.E., Mulhearn, T.O., 1956. An experimental investigation of the deformed zone associated with indentation hardness impressions. J. Mech. Phys. Solids 5, 125–134.

Suresh, S., 1998. Fatigue of Materials, Second ed. Cambridge University Press, Cambridge.

Tabor, D., 1951. The Hardness of Metals. Oxford University Press, Oxford.

Tirupataiah, Y., Sundararajan, G., 1987. A comprehensive analysis of the static indentation process. Mater. Sci. Eng. 91, 169–180.

Tirupataiah, Y., Sundararajan, G., 1991. On the constraint factor associated with the indentation of work-hardening materials with spherical ball. Metall. Trans. 22A, 2375–2384.

Tirupataiah, Y., Sundararajan, G., 1994. The strain-rate sensitivity of fbw strss and strain-hardening rate in metallic materials. Mater. Sci. Eng. A 189, 117–127.

Weber, G.G.A., 1988. Computational procedures for a new class of finite deformation elastic–plastic constitutive equations. Ph.D. Dissertation, MIT.

Weber, G.G., Lush, A.M., Zavaliangos, A., Anand, L., 1988. An objective time integration procedure for isotropic rate-independent and rate-dependent elastic–plastic constitutive equations. Int. J. Plast. 6, 701–744.

White, C.S., 1988. A combined isotropic–kinematic hardening model for large deformation metal plasticity. Ph.D. Dissertation, MIT.

White, C.S., Bronkhorst, A., Anand, L., 1990. An improved isotropic–kinematic hardening model for moderate deformation metal plasticity. Mech. Mater. 10, 127–147.

Yu, W., Blanchard, J.P., 1996. An elastic–plastic indentation model and its solution. J. Mater. Res. 11, 2358–2367.